A Non-Natural Wurtzite Polymorph of HgSe: A Potential 3D Topological Insulator

Daniel Dumett Torres,[†] Progna Banerjee,[‡] Sudhakar Pamidighantam,[§,||] and Prashant K. Jain[*,†,‡]

[†]Department of Chemistry, University of Illinois at Urbana−Champaign, Urbana, Illinois 61801, United States
[‡]Department of Physics, University of Illinois at Urbana−Champaign, Urbana, Illinois 61801, United States
[§]Science Gateways Group, Research Technologies, Indiana University, Bloomington, Indiana 47408, United States
[||]National Center for Supercomputing Applications (NCSA), University of Illinois at Urbana−Champaign, Urbana, Illinois 61801, United States

S *Supporting Information*

ABSTRACT: This article demonstrates the power of topotactic synthesis coupled with density functional theory (DFT) for accessing and exploring new phases of matter. Naturally occurring HgSe is a semimetal with a zero gap. Unlike this natural zincblende form of HgSe, our DFT investigations predict that wurtzite HgSe has both an inverted band structure and a band gap, making it a 3D topological insulator (TI). Calculated band structures of $Hg_xCd_{1-x}Se$ alloys containing strongly relativistic Hg and weakly relativistic Cd show that band gap opening is a consequence of symmetry breaking resulting from a combination of crystal anisotropy and the scalar relativistic effect of Hg electrons. The relativistic contribution of Hg is significant enough in alloys with $x \geq 0.33$ for achieving 3D TI behavior at room temperature. We experimentally realize the non-natural wurtzite form by topotactic ion exchange of wurtzite CdSe nanocrystals (NCs), which yields alloy NCs in the range $x = 0-0.54$ whose measured band gaps follow the predicted trend. We introduce crystal anisotropy as a new handle for expanding the classes of TI materials and also shed light on electronic principles in nanocrystalline alloys containing relativistic metals. NCs of this new wurtzite phase can become platforms for discovery of rich topological states and properties.
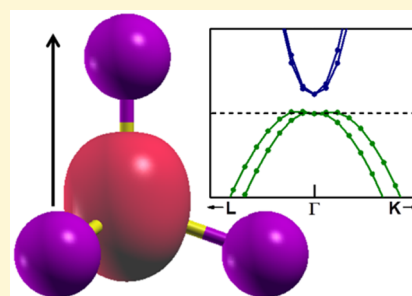
INTRODUCTION

Topological insulators (TIs) represent a novel state of matter: the bulk (3D) of a TI is electrically insulating, but the surface (2D) contains topologically protected conductive states.[1,2] TI materials are receiving surging interest as platforms for discovery of exotic condensed matter phenomena, e.g., Majorana fermions,[3−5] and for the utility of the spin-protected surface conduction in spintronics and quantum computing.[6−9] Most materials that are intrinsically 3D topological insulators are Bior Sb-based, in particular selenides and tellurides of these metals. The list of materials is, however, rather small. Expansion of the class of 3D TI materials can accelerate new findings and technological applications. Mercury chalcogenides represent potential candidates[10] due to strong spin−orbit coupling effects associated with heavy Hg. For instance, HgTe/HgCdTe quantum wells have exhibited 2D TI properties with spin-protected 1D edge states. But intrinsic (in the absence of strain or external fields) 3D TI behavior is not known in mercury chalcogenides. For a solid to be a 3D TI, two conditions need to be met:[6,7,11−16] (i) a nontrivial band structure: the conduction and valence bands are inverted, which results in the helical spin-protected surface conduction states, and (ii) a nonzero band gap so that the bulk is electrically insulating. Here, we find using electronic structure simulations a non-natural polymorph of HgSe, which unlike hitherto known

phases[17,18] satisfies these conditions and qualifies as a 3D TI. We experimentally realize this novel crystal phase in nanocrystals (NCs) via the topotactic method of synthesis, cation exchange.[19−22]

HgSe, which has been studied extensively since the 1960s,[23] has a zincblende crystal structure[24] and a nontrivial, inverted band structure.[23,25,26] However, zincblende HgSe has a zero gap and is therefore classified as a Weyl semimetal (similar to α-Sn and HgTe) and not a 3D TI. Our density functional theory (DFT) investigations reveal that unlike the known zincblende form, a non-natural wurtzite polymorph of HgSe has a finite band gap in addition to inverted bands, making it a 3D TI. We synthesize using cation exchange this novel wurtzite polymorph in the form of $Hg_xCd_{1-x}Se$ alloy NCs, allowing a systematic experimental and theoretical investigation of the band gap as a function of composition. Alloys with a Hg fraction ≥0.33 fall within the room-temperature 3D TI regime. Band gap and electronic structure trends in this alloy system show that the 3D TI is a consequence of the scalar relativistic contribution of the heavy Hg nuclei[26] combined with the crystal anisotropy of the wurtzite structure. Thus, we introduce crystal anisotropy as a
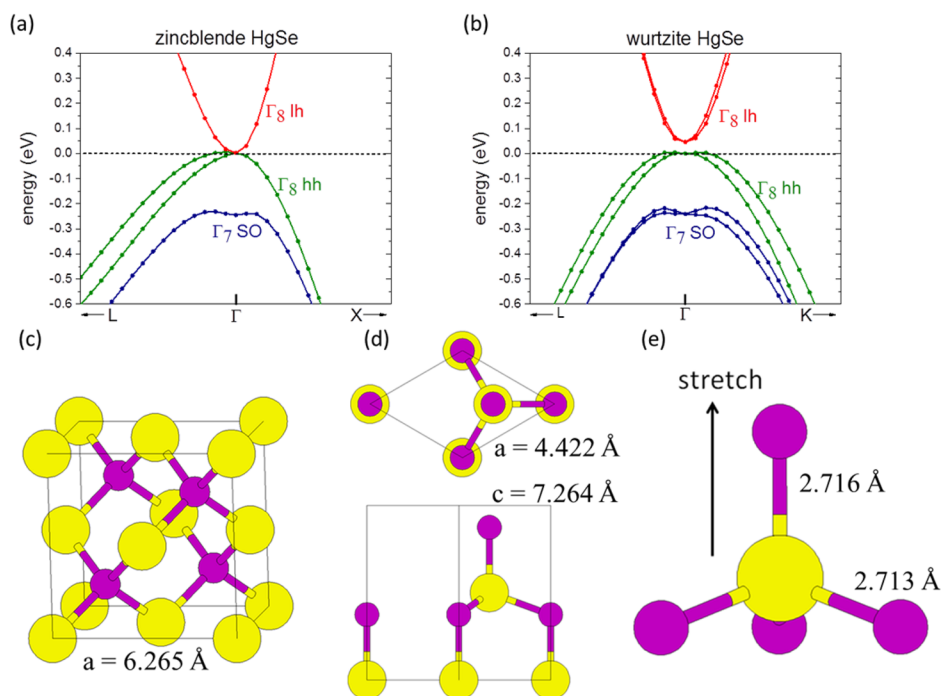
Figure 1. Band structures and unit cell structures of zincblende and wurtzite HgSe. (a) Our calculated band structure of zincblende HgSe. (b) Our calculated band structure of wurtzite HgSe, indicating the presence of a band gap ~46 meV. In panels a and b, we assigned light hole (Γ_8 lh), heavy hole (Γ_8 hh), and split off (Γ_7 SO) bands in a simplified manner based on zincblende semiconductors.[27] Lower lying bands are not included. (c) Unit cell representation for the natural zincblende phase of HgSe in which every Hg^{2+} is coordinated tetrahedrally to four Se^{2-} anions through bonds of equal length. (d) Unit cell representation of the novel wurtzite phase of HgSe in which Hg and Se are tetrahedrally bonded to one another, but as shown in panel e, one of the tetrahedral bonds is slightly longer than the other three, introducing a crystal anisotropy along the so-called c axis direction. For panels c−e, calculated lattice parameters and bond lengths are indicated.

new handle for controlling topological properties and also elucidate the principles behind electronic band structure tuning achieved by alloying of strongly and weakly relativistic metals in ionic solids.

■ RESULTS AND DISCUSSION

Crystal Anisotropy and Band Gap Opening. To study the effects of crystal structure on the electronic properties of HgSe, we used periodic plane-wave basis DFT with spin orbit-coupling as implemented in the Quantum Espresso software suite.[28] Our DFT calculations of zincblende HgSe (Figure 1a) confirm that it has an inverted band structure as has been demonstrated in the past with experiment and theory.[23,25,26] The band structure can be contrasted with the typical zincblende semiconductors, e.g. CdSe, wherein the lowest energy conduction band is comprised of cation s-orbitals, whereas the highest energy valence bands, i.e., light hole (Γ_8 lh) and heavy hole (Γ_8 hh), are comprised of the anion p-orbitals. HgSe, however, has a dramatically different band structure due to the relativistic nature of the electrons of the heavy Hg. In HgSe, the band comprised of Hg s-like states is significantly lowered in energy due to the relativistic contraction of the outermost 6s-orbitals of Hg. The cation s-like band thus becomes a deeper lying valence band. The Γ_8 lh and Γ_8 hh bands become the lowest energy conduction and highest energy valence bands, respectively. Because these two bands are degenerate in the zincblende structure at the Γ point, HgSe lacks a band gap and is therefore only a topological semimetal.

Realization of TI behavior in HgSe would require a finite gap between the Γ_8 lh and Γ_8 hh bands at the Γ point. Gap opening could be achieved by lifting of the degeneracy of these bands.

Such degeneracy breaking is exhibited in wurtzite CdSe due to anisotropic crystal field splitting;[29] therefore, we were motivated to investigate the wurtzite form of HgSe even though such a form is not known to exist naturally. The calculated band-structure of this wurtzite polymorph is shown in Figure 1b. We find that the inverted band structure is maintained in the wurtzite form with Γ_8 lh and Γ_8 hh bands as the conduction and valence band edges, respectively. However, these two bands are no longer equivalent in energy at the Γ point, resulting in a nonzero band gap. The band gap is 46 meV in magnitude. As we explain below, this band gap opening is indeed a consequence of crystal anisotropy in the wurtzite phase (Figure 1e), which operates in a manner similar to the application of a uniaxial strain to zincblende HgSe.[15,28,30]

Hg^{2+} and Se^{2-} in the wurtzite phase are tetrahedrally coordinated as in the zincblende case. However, there is a key difference between the two structures: all four Hg−Se bonds are of equal length in the zincblende phase (Figure 1c), whereas in wurtzite (Figures 1d and e), the Hg−Se bond, i.e., the one along the c-axis of the crystal, is elongated. This small elongation breaks the degeneracy of the Γ_8 lh and Γ_8 hh bands. To understand this effect, the charge density maps for these two bands are compared in Figure 2. Although both bands are comprised of linear combinations of the Se p orbitals, the charge density maps show that the Γ_8 lh band differs in symmetry from the Γ_8 hh band in both crystal phases. The Γ_8 hh band is directed along the c-axis (of the wurtzite crystal), whereas the Γ_8 lh band is oriented in a plane normal to this axis.

In the zincblende phase, the energy of the Se p orbitals is not orientation dependent due to the equivalence of the four
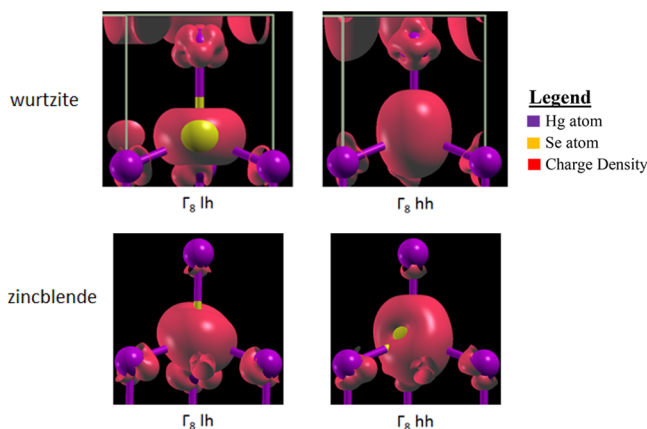
Figure 2. Charge density maps for the lowest energy conduction band, Γ_8 lh (left), and highest energy valence band, Γ_8 hh (right), of wurtzite (top) and zincblende (bottom) HgSe.

tetrahedral bonds. The valence bands comprised of a linear combination of p_x, p_y, and p_z orbitals are triply degenerate at the Γ point in the perfect tetrahedral coordination of the zincblende phase, in the absence of spin−orbit coupling.[30] Spin−orbit coupling results in the Γ_7 SO band being split off in energy from the Γ_8 hh and Γ_8 lh bands, but the latter two remain degenerate at the Γ point. This twofold degeneracy follows the conventional zincblende band structure,[31] except that due to band inversion in zincblende HgSe, this twofold degeneracy occurs between the highest lying valence band (Γ_8 hh) and the lowest lying conduction band (Γ_8 lh), leading to a zero gap (Figure 1a).

In the anisotropic wurtzite structure, the strength of the crystal field experienced by a Se p orbital depends on the orbital orientation. The crystal field degeneracy between the p_x, p_y, and p_z states is broken.[30] Se p-like states oriented along the elongated bond experience reduced electrostatic repulsion from cation electrons and are therefore stabilized with respect to Se p-like states of other orientations. Thus, the Γ_8 hh band, oriented along this elongated band, is lowered in energy relative to the Γ_8 lh band at the Γ point, thereby opening a gap. The crystal field splitting energy difference between the Γ_8 lh and Γ_8 hh bands corresponds to the magnitude of this band gap.

Conventional semiconductor band gaps calculated using the Perdew−Burke−Ernzerhof (PBE) functional are known to be underestimated due to self-interaction errors.[32] However, crystal field splitting energy differences are computed more accurately by DFT, possibly due to cancelation of self-interaction errors. For instance, the crystal field splitting difference between the lh and hh bands in wurtzite CdSe is estimated to be 35 meV by our DFT calculations (Figure S2a), which is close to the known experimental value of 29 meV.[33] The close agreement further suggests that our relaxed geometries are representative of the actual bond elongation present in the wurtzite phase. Because the band gap of wurtzite HgSe is equal to the crystal field splitting energy difference between the Γ_8 lh and Γ_8 hh bands, our calculated band gap of 46 meV can be expected to be quantitative. The calculated band gap is sufficiently larger than thermal broadening at room temperature (25 meV), which predicts electrically insulating behavior in the bulk at room temperature. Cryogenic cooling would not be required for realizing 3D TI behavior. These predictions motivated us to synthesize this non-natural wurtzite polymorph of HgSe.

Realization of the Wurtzite Structure in NCs. For our synthesis of wurtzite HgSe, we employed cation exchange, which is a method being increasingly used to produce NCs in novel shapes, morphologies, and phases.[20,34−45] In this method, cations of a colloidal ionic NC are replaced by another cation, while the anionic sublattice is maintained intact, often resulting in (metastable) crystal structures dictated by the initial template rather than by equilibrium phase diagrams.[20,36,46] We exploited this topotactic manner of synthesis[21,36,45,47] by starting with wurtzite CdSe NCs as templates and exchanging the Cd^{2+} ions with Hg^{2+} at room temperature.[48] Note that CdSe NCs have been subject to exchange with Hg^{2+} in the past.[24,49−51] In the well-studied cases, the starting CdSe template was zincblende,[49,50] and naturally, the resulting product was not wurtzite. In one study on wurtzite CdSe nanorods,[51] although clear crystallographic evidence was missing, the product was suggested from scanning transmission electron microscopy (STEM) to contain local regions of zincblende HgSe. However, the conditions under which the exchange was performed were markedly different from our synthetic method (see Methods). Aqueous, basic conditions were employed in this past work with water-soluble mercaptopropionic acid-coated CdSe nanorods. A $Hg(ClO_4)_2$ salt and a large Hg/Cd ratio of 60 was employed for the exchange reaction, which was allowed to proceed for 4 days prior to STEM characterization. Under these conditions, the Hg distribution varied significantly across the product nanorods: although the overall exchange conversion was limited to $x = 0.1$, some regions of the nanorods were significantly Hg-enriched. Nucleation of zincblende HgSe, which requires drastic reorganization of the more rigid Se sublattice, occurred in the regions with high Hg enrichment, significantly past the miscibility limit of HgSe in CdSe; however, such domains were not widespread. Summarizing current literature, there is no finding of a dominant wurtzite product in past studies of Hg^{2+} exchange of CdSe.

The outcome of our synthesis was a series of $Hg_xCd_{1-x}Se$ alloy NCs in the novel wurtzite phase, as found by detailed characterization. The transformation from CdSe to HgSe was carried out on NCs as opposed to bulk samples due to mass-transport-related bottlenecks in exchange reactions on the bulk scale.[45] The chemical composition of the NCs at various stages of the exchange was determined by inductively coupled plasma atomic emission spectroscopy (ICP-AES). The results (Table 1) show successful replacement of Cd^{2+} with Hg^{2+}. High-

Table 1. Elemental Composition of Initial, Intermediate, and Final NCs Obtained by ICP-AES

sample	Cd (mass %)	Hg (mass %)	Hg/(Hg + Cd) atomic ratio (x)
CdSe	22.06	0.65	0.01
Int 1	11.03	3.67	0.16
Int 2	9.51	8.59	0.34
final	4.86	10.16	0.54

resolution transmission electron microscopy (HRTEM) showed that the throughout the exchange process, the quasi-spherical morphology was maintained (Figure S1). The initial CdSe NCs (peak diameter ~3.6 nm) were similar in size as the final product NCs (peak diameter ~3.9 nm).

The powder X-ray diffraction (PXRD) pattern did not show appreciable change over the course of the exchange, indicating that the wurtzite crystal structure was retained (Figure 3c). PXRD simulations (Figure 3d) assuming a topotactic
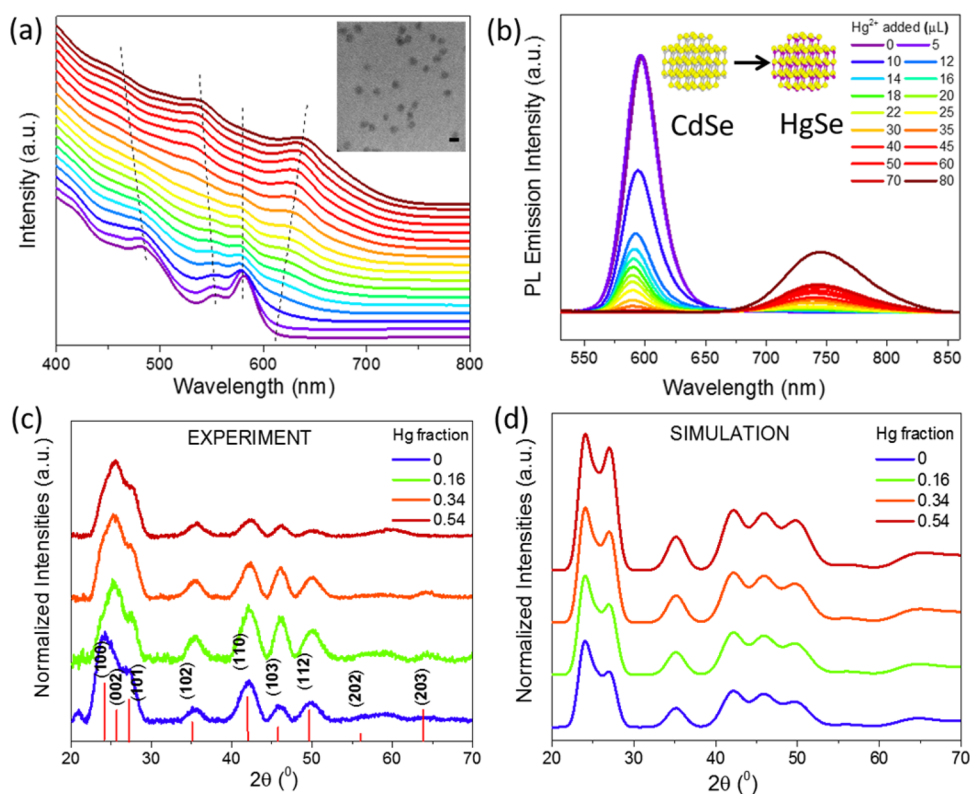
Figure 3. Topotactic cation exchange from wurtzite CdSe to $Hg_xCd_{1-x}Se$. (a) Absorbance spectra (stacked for presentation) for NCs in the course of the exchange. Inset shows an HRTEM image of the furthest exchanged NCs (scale bar = 5 nm). Dotted lines guide the eye to the emergence of the exciton peak associated with HgSe formation (the reddest peak) and the disappearance of the exciton peaks associated with CdSe in the course of the titration. (b) PL emission spectra obtained at various stages in the course of the stepwise cation exchange from CdSe to $Hg_xCd_{1-x}Se$ NCs. For both panels a and b, the amount of Hg^{2+} solution added at each stage in the titration is indicated in the legend in panel b. (c) PXRD patterns obtained at the initial, intermediate, and the final stages. The Hg to metal fraction, x, indicated in the legend is based on the elemental composition measured by ICP-AES and tabulated in Table 1. Reference reflections for bulk wurtzite CdSe (ICSD no. 41825) as are indicated by red sticks. (d) Simulated PXRD patterns for wurtzite $Hg_xCd_{1-x}Se$ NCs for the different Hg fractions, x, corresponding to those in the experiment. Patterns in panels c and d were stacked vertically for presentation purposes.

replacement of Cd^{2+} with Hg^{2+} reproduce the experimental observations. In the experimental PXRDs, there are slights shifts in the peaks as one goes from the initial NCs to the final ones: e.g., the {102} reflection shifts from $2\theta = 35.2$ to $35.6°$, and the {110} reflection shifts from $2\theta = 42.1$ to $42.5°$. These shifts amount only to small, ca. 1%, lattice constant changes as wurtzite CdSe NCs are transformed to wurtzite $Hg_xCd_{1-x}Se$ NCs. The near-preservation of the lattice dimensions is consistent with our DFT simulations, which show identical lattice constants ($a = 4.422$ Å, $c = 7.264$ Å) for structurally relaxed wurtzite CdSe and wurtzite HgSe cells. The finding is also consistent with the known zincblende phase of HgSe, which has a near-identical structure and lattice constant (6.085 Å) as zincblende CdSe.[52] The similarity of the lattice structure and lattice parameters of wurtzite HgSe and wurtzite CdSe also make us favor progressive alloying rather than a shrinking CdSe core/thickening HgSe shell mechanism of exchange. However, the conclusion of topotactic formation of wurtzite $Hg_xCd_{1-x}Se$ stands irrespective of the mechanism.

We also followed the replacement of Cd^{2+} by Hg^{2+} in the NC lattice by UV–vis absorbance (Figure 3a) and photoluminescence (PL) emission (Figure 3b) spectrophotometry. It is well-known that CdSe NCs have a very well-defined optical signature which can be tuned by doping.[34,53,54] The exchange with Hg^{2+} results in the gradual disappearance of the exciton peaks of CdSe NCs (first exciton peak at 580 nm). There is

concomitant appearance of a new exciton peak (600−650 nm region) that can be associated with $Hg_xCd_{1-x}Se$ formation. This new exciton peak red-shifts with increasing conversion, x. In PL spectra, the band centered at 600 nm, associated with band gap emission of CdSe NCs, slightly blue-shifts and decreases in intensity until it is fully extinguished. Concomitantly, a new PL band centered around 750 nm emerges and increases in intensity. This new band, which could be associated with band gap emission of $Hg_xCd_{1-x}Se$ NCs, is seen to red-shift with increasing Hg conversion, x. The point at which the spectra do not show any further changes was defined as the final stage. The elemental composition of the final NCs shows significant residual Cd and an Hg fraction of 0.54. Even with elevated temperatures and a huge excess of the Hg^{2+} salt, complete conversion to HgSe was not observed. Thus, the exchange appears to be self-limited, akin to a previous report on the cation exchange of PbSe nanocrystals to CdSe[55,56] which, like the reaction system studied here, involves cation exchange between two divalent cations, known to be kinetically challenging. Conversion to Hg-rich compositions may require the nucleation of the stable, zincblende form of HgSe. Such nucleation would involve drastic reorganization of the rigid Se lattice and would therefore be expected to be kinetically limiting despite the availability of sufficient Hg^{2+}.

**Alloying Effects on Electronic Structure.** While our synthesis successfully accessed the wurtzite phase, the
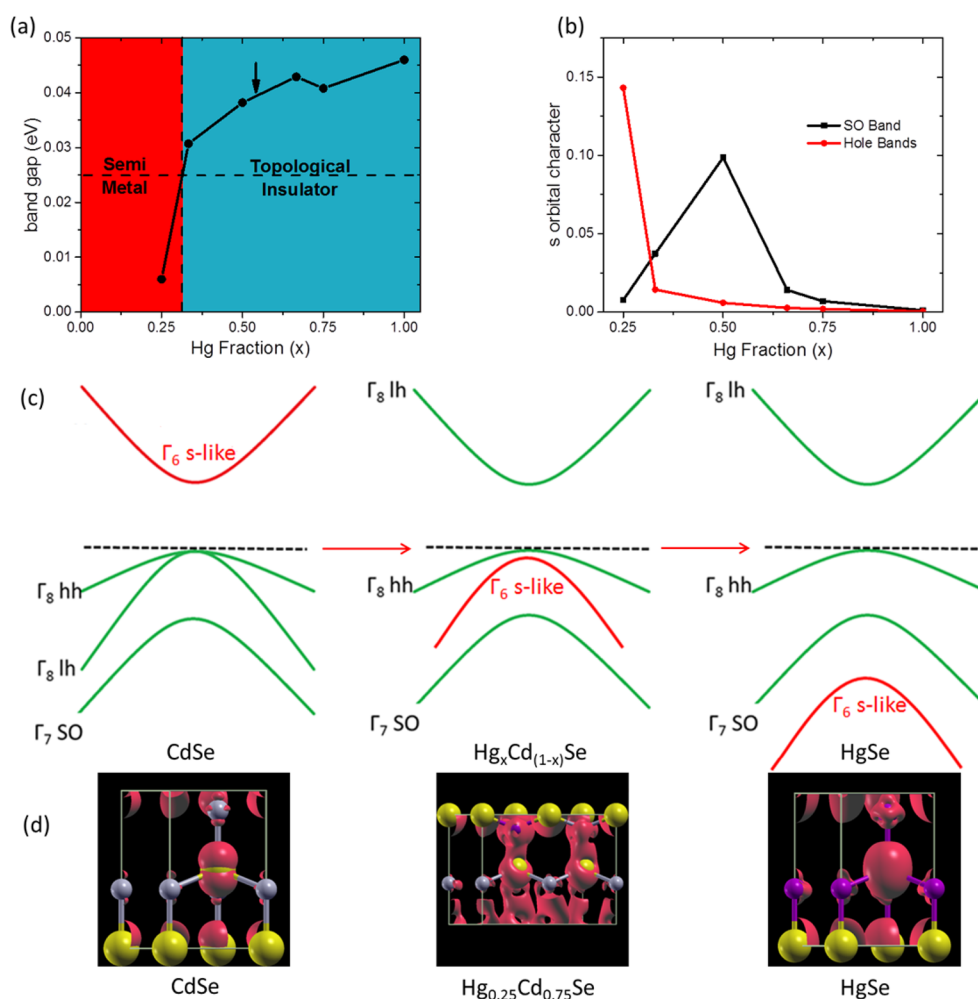
Figure 4. Overview of alloying trends in electronic structure of $Hg_xCd_{1-x}Se$. (a) Dependence of the calculated band gap on the Hg fraction, x, of the alloy. The arrow marks the furthest extent to which alloying has been achieved in our Cd^{2+} to Hg^{2+} cation exchange experiments. The horizontal dotted line marks the magnitude of thermal broadening at room temperature, which allows demarcation of the regime of room temperature 3D TI behavior (cyan) from that of topological semimetal behavior (red). (b) The cation (combination of Hg^{2+} and Cd^{2+}) s orbital character contribution to the frontier bands as a function of x. "SO band" refers to the Γ_7 SO band, and "Hole Bands" refers to the combination of the Γ_8 lh and Γ_8 hh bands, which are treated as one for this analysis. (c) Schematic of the band structure showing inversion and then shift of the Γ_6 s-like band downward in energy as heavy Hg nuclei are incorporated into a CdSe lattice. (d) Calculated charge density maps for the Γ_8 hh band at representative compositions. At the pure CdSe and HgSe end points, the Γ_6 s-like band is well-separated in energy from the Γ_8 hh band and does not donate any s character to the Γ_8 hh band. However, at intermediate compositions such as in $Hg_{0.25}Cd_{0.75}Se$, significant cation s character can be observed in the Se p dominated Γ_8 hh band.

incomplete exchange of Cd^{2+} with Hg^{2+} led us to investigate how the remaining Cd^{2+} in $Hg_xCd_{1-x}Se$ alloy compositions influences the band structure and the band gap. In particular, we needed to determine whether or not a $Hg_xCd_{1-x}Se$ alloy has attributes of a 3D TI at room temperature, similar to HgSe. Systematic calculations of the electronic structures of wurtzite $Hg_xCd_{1-x}Se$ alloys were performed over the full range $x = 0-1$ (Figures 4 and S2).

The key trends are as follows. Wurtzite CdSe ($x = 0$) has a trivial band structure, i.e. there is no band inversion, and the lowest energy Γ_6 band conduction band is comprised mainly of Cd s orbitals. As the structure is alloyed with Hg, the relativistically contracted 6s orbital of Hg contributes to the Γ_6 band and lowers it in energy (Figure 4c). Already at $x = 0.25$, this relativistic contribution of Hg is large enough for the Γ_6 band to cross below the Γ_8 bands in energy, resulting in band inversion wherein the Γ_8 lh and Γ_8 hh bands take the role of the lowest energy conduction and highest energy valence bands,

respectively. A small band gap (6 meV) is seen at $x = 0.25$. The band structure continues to remain inverted up to HgSe, and the band gap increases at room temperature (25 meV). Thus, wurtzite $Hg_xCd_{1-x}Se$ alloys with 33% or greater Hg fractions have the band structure attributes of a room temperature 3D TI. Our experimentally synthesized alloy NCs with 54% Hg fall well within the 3D TI regime at room temperature (cyan region in Figures 4a).

Next, we elucidate the electronic origin of the band gap trend. With increasing x, the Γ_6 band owing to its cation s character continues to move lower in energy due to the increasing relativistic contribution of Hg. In its progressive energy downshift with increasing x, the Γ_6 band crosses energetically with other bands in sequence. Near about $x = 0.25$, the Γ_6 band becomes similar in energy to the Γ_8 bands, which imparts the Γ_8 bands with a significant cation s-like character (Figures 4b and d). As the Hg fraction is increased from $x = 0.25$ to 0.5, the Γ_6 band moves energetically away
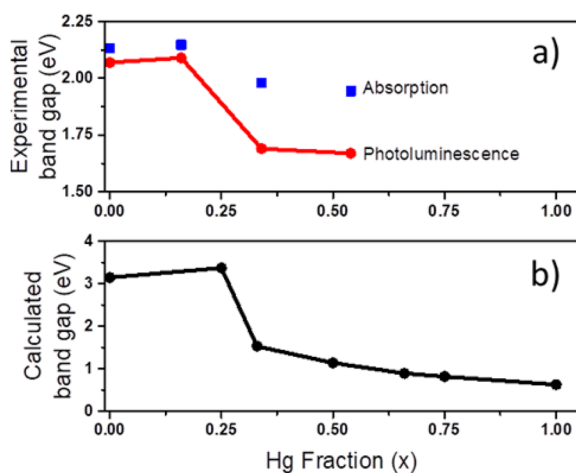
x	m_h*/m	m_e*/m	$E_{NP\ gap}$ (eV)
0.00	0.83	0.08	3.14
0.25	0.81	0.04	3.37
0.33	2.13	0.08	1.53
0.50	1.20	0.11	1.14
0.66	2.15	0.14	0.89
0.75	1.76	0.16	0.82
1.00	1.36	0.23	0.63

Figure 5. Experimental (a) and calculated (b) band gaps for 3.5 nm NCs of varying Hg fraction. Experimental (optical) band gaps plotted here are based on peak maxima obtained from absorption (blue dots) and PL emission (red squares) spectra. Calculated band gaps follow eq 2. Table on the right-hand side provides the effective carrier masses in terms of the free electron mass used for NC size correction. The experimental trend agrees qualitatively with the calculated one, most notably with regard to the sharp decrease in NC band gap about $x = 0.25$. However, it must be acknowledged that the match is not quantitative: the calculated NC band gap decreases by 55% from 3.37 eV ($x = 0.25$) to 1.53 eV ($x = 0.33$), whereas from PL, the NC band gap drops by 20% from 2.09 eV ($x = 0.16$) to 1.69 eV ($x = 0.34$). The quantitative discrepancy can be attributed to limitations of the calculation model. In addition to errors associated with treatment of electron correlation and self-interaction in DFT of semiconductors, there are considerable errors associated with the treatment of NC size effects. Effective masses calculated on the basis of band dispersion are not quantitative for NCs, in which well-defined bands do not exist, and the use of an effective mass model can be a severe approximation. In addition, at each point in our exchange reaction, the alloy composition can be variable across the NC sample; the measured Hg fraction x represents only an average. This can lead to quantitative discrepancy with the calculated band gap, as explained in Figure S5.

from the Γ_8 bands and approaches the deeper lying Γ_7 SO band. As a result, the cation s character of the Γ_8 bands decreases, and that of the SO band increases. At $x = 0.5$, the Γ_6 band crosses the SO band, and the latter exhibits a maximum in its cation s character (Figure 4b).

In HgSe, the Γ_6 band, comprised of the relativistically stabilized Hg 6s states, is deep within the valence band, and neither the Γ_8 band nor the Γ_7 SO band have any significant cation s character, and Se p character dominates. As the fraction of Cd increases and that of Hg decreases ($x = 1$ to 0.25), the Γ_8 lh and Γ_8 hh bands increase in their cation s (isotropic) character and concomitantly decrease in their Se p character (Figure S3). As a result of the reduced directional nature of the Γ_8 lh and Γ_8 hh bands, the effect of crystal field splitting anisotropy decreases, and the Γ_8 lh and Γ_8 hh bands become closer in energy at the Γ point, i.e., the band gap decreases. Although this effect explains the overall decrease in the bulk band gap as the Hg^{2+} fraction goes from $x = 1$ to 0.25 (Figure 4a), there is an anomalous increase in the band gap when going from $x = 0.75$ to 0.66. We attribute this anomaly to a different kind of anisotropy. Unlike pure HgSe, the intermediate compositions can have an additional anisotropy resulting from the ordering of Cd^{2+} and Hg^{2+} in separate, alternating layers. The resulting compositional anisotropy can contribute to symmetry breaking (between the Γ_8 lh and Γ_8 hh bands) and enhance the magnitude of the band gap. The evidence for such an effect is found in a system with no crystallographic anisotropy, i.e., a zincblende lattice (Figure S4). In zincblende HgSe, all Se p states experience the same crystal field interaction; the lh and hh bands are degenerate, and a zero gap is calculated. But in zincblende $Hg_xCd_{1-x}Se$, a small few meV band gaps can be observed due solely to this alloying-induced compositional anisotropy. The predicted band gap is maximum in magnitude near $x = 0.5$ because a 1:1 Hg:Cd

composition allows for the greatest degree of layer-wise stratification within the crystal.

Lastly, we validate our computational predictions by comparing DFT-calculated band gaps with those measured optically for the range of $Hg_xCd_{1-x}Se$ alloys accessed in our synthesis (Figure 5). Because our synthesized materials consist of ~3.5 nm NCs, we must account for the effect of size-dependent quantum confinement and exciton binding energy on the optical gaps.[57] Because the wurtzite phase of $Hg_xCd_{1-x}Se$ is realized for the first time here, carrier transport properties are naturally unavailable. We determined electron and hole effective masses from our band structure calculations as

$$m^* = \left| \frac{\hbar^2}{\partial^2 E/\partial k^2} \right| \tag{1}$$

where E represents the band energy and k indicates the crystal momentum. We accounted for carrier confinement using the effective mass approximation[58−61] and included an exciton binding energy correction in our estimation of the size-modified optical band gap, $E_{NP\ gap}$ as

$$E_{NPgap} = E_{bulkgap} + \frac{\hbar^2}{2R^2}\left(\frac{1}{m^*_e} + \frac{1}{m^*_h}\right) - \frac{1.786e^2}{4\pi\varepsilon_{QD}\varepsilon_0 R} \tag{2}$$

where $E_{bulk\ gap}$ is the calculated band gap for the bulk alloy, m^*_e and m^*_h are the electron and hole effective masses, respectively, and R is the NC radius, fixed at 1.75 nm. While it is difficult to obtain an exact quantitative match, there is qualitative agreement between the calculated trends and the experimentally determined ones: (i) Cd-rich NC compositions between $x = 0$ and 0.25 have band gaps in the visible region which increase marginally with increasing x. (ii) Between $x = 0.25$ and 0.33, the band gap drops sharply, and (iii) sufficiently Hg-exchanged

NCs (x = 0.33 to 1.0) have near-infrared band gaps, which decrease in magnitude gradually with increasing x.

Unlike the bulk band gaps which reflect the solid band structure (Figure 4a), NC band gaps are strongly dominated by carrier confinement effects. Therefore, to understand the trend in NC band gaps across alloy composition, one needs to examine the change in carrier properties, especially effective electron masses, which are smaller (Figure 5, table) and therefore dominate the confinement effect in the NCs (eq 2). With increasing Hg fraction, above x = 0.25, the inverted Γ_6 band moves lower in energy, leading to a decreasing Hg s contribution to the lowest energy conduction band. These changes in the orbital nature of the conduction band result in an increase in the effective electron mass and thereby a decrease in the NC band gap with increasing Hg fraction.

CONCLUSIONS

Thus, our DFT simulations reveal that the wurtzite polymorph of HgSe has a remarkably different electronic structure from that of the naturally known zincblende phase of HgSe. While zincblende HgSe is a semimetal, the wurtzite polymorph has the attributes of a 3D TI insulator, including band inversion and a nonzero band gap. Motivated by the calculations, we successfully realize this non-natural wurtzite phase by topotactic exchange of Cd^{2+} in wurtzite CdSe NCs with Hg^{2+}. We measured band gaps of the synthesized wurtzite $Hg_xCd_{1-x}Se$ alloy NCs and find a trend in agreement with our simulations. Systematic electronic structure investigations of the $Hg_xCd_{1-x}Se$ alloys elucidate the physical principles underlying 3D TI behavior. Band inversion is a result of the scalar relativistic effect of Hg 6s electrons on the Γ_6 band, while band gap opening is the result of symmetry breaking due to the crystalline anisotropy of the wurtzite structure. The relativistic contribution of Hg is sufficient for alloys with $x \geq 0.33$ to demonstrate attributes of 3D TIs at room temperature. Thus, we introduce crystal anisotropy as a new handle for tuning band topology, elucidate the important role of scalar relativistic effects, and expand of the class of materials with 3D TI attributes to include mercury chalcogenides.

Direct demonstration of spin-protected conductive surface states via angle-resolved photoemission spectroscopy (ARPES) or scanning tunneling microscopy (STM) still remains to be conducted. A single crystal with low defect concentration is required for such measurements. NCs themselves may not serve the purpose: NCs do not have well-defined bands and (surface and bulk) band topology characteristics do not directly translate from bulk, semi-infinite solids to nanosized ones. However, these NCs can be employed as precursors for realizing a bulk 3D TI: surface ligands can be removed, and NCs can be assembled into a mesoscopic or macroscopic supersolid while maintaining the wurtzite phase with 3D TI property. Second, despite their lack of bands, which may preclude 3D TI behavior, NCs can exhibit other allied phenomena such as low-dimensional topological states (an example includes recently found 1D spin-polarized states along step edges on the surface of a TI[62]) or previously unknown exotic phenomena. Faceting, surface curvature, ligands, crystal anisotropy, and quantum confinement can add further richness. Therefore, NCs of this wurtzite phase can become platforms for discovery of new topological states and properties.[62–65]

METHODS

Experimental Methods. *Synthesis of ca. 4 nm wurtzite CdSe NCs.* Wurtzite CdSe NCs of ca. 4 nm size were synthesized as per Carbone et al.[48] and also described in White et al.[19] Cadmium oxide (0.06 g), octadecylphosphonic acid (0.28 g), and trioctylphosphine oxide (3.0 g) were added to a 50 ml three-neck round-bottom flask. A solution of trioctylphosphine (TOP)-Se was prepared in a glovebox by dissolving 0.6 g Se in 4.48 mL TOP and stirring the solution at room temperature overnight. The reaction flask was degassed under vacuum at 150 °C for 1.5 h. The flask was then put under Ar atmosphere, and the temperature was gradually increased to 300 °C over the course of 2 h. When the temperature was slowly further ramped up to 320 °C, the solution became optically clear. After reaching 320 °C, 1.8 mL of TOP was gradually injected into the mixture. The temperature of the mixture in the flask was raised to 360 °C, and then 0.45 mL of the TOP-Se solution was injected rapidly. After injection, the solution was heated at 360 °C for 40 s or until the solution was a bright red color, after which the heating mantle was removed. The NC colloid obtained from the synthesis was washed with toluene and methanol multiple times and finally dispersed in toluene.

Cation Exchange of CdSe NCs with Hg^{2+}. CdSe NCs were dispersed in hexane with ligands (0.7 mL oleic acid and 0.7 mL oleylamine) added to aid colloidal stability over the course of exchange. To this NC colloid (OD_{580} nm ~0.8) placed in a sealed quartz cuvette was added a solution of 16 mg of mercury acetate in 2 mL of octylamine in few-microliter aliquots with vigorous stirring at room temperature. Cation exchange was monitored by UV−vis absorbance and PL emission spectrophotometry. PL emission spectra were obtained with a 450 nm excitation wavelength. The intermediates were chosen from the UV−vis absorbance data: the stage at which the exciton peak corresponding to HgSe just began to emerge was labeled as intermediate 1 (I1). A second stage at which a clear exciton peak from HgSe was seen in coexistence with a weak CdSe exciton was labeled as intermediate 2 (I2). I1 and I2 correspond to specific points in the titration after 12 and 20 μL of the Hg^{2+} solution are added, respectively.

Electron Microscopy Characterization. HRTEM images were acquired on a JEOL 2010 EF-FEG operating at 200 kV. Samples were prepared by drop casting an NC solution onto an ultrathin carbon grid followed by washing of the grid with methanol. The sample-coated grids were then desiccated under vacuum overnight to volatilize excess ligands. NC size analysis was performed on HRTEM images using the software Fiji. Sizes of the quasi-spherical NCs were determined manually.

Elemental Composition Analysis. ICP-AES was used for determination of the elemental compositions of the NCs at different stages: the initial CdSe NCs, intermediates I1 and I2, and the final product NCs. For preparation of each sample for ICP-AES, the NC colloid in hexane was purified by three cycles of washing in methanol and centrifugation. The final centrifuged pellet was subsequently dried in a quartz digestion tube by flowing N_2 gas. Approximately 8 mg of the initial CdSe NCs, 7 mg each of the intermediates, and 12 mg of the final exchanged sample were subject to ICP-AES, and Cd, Hg, and Se weight percentages were measured. The elemental composition is tabulated in Table 1.

PXRD Characterization. Samples for PXRD measurements were prepared by drop-casting NCs from colloidal solution into a thick film on a zero-background quartz substrate. PXRD patterns were collected on a Rigaku Miniflex 600 powder X-ray diffractometer operated at full power (40 kV - 15 mA) with Cu K_α radiation with an X-ray wavelength of 1.54 Å. Diffraction was collected in reflection mode in the 2θ = 20−75° range using a step size of 0.04°. Diffraction patterns were plotted in Origin Lab software, and a baseline subtraction was performed to emphasize the diffraction peaks. Reference reflections for the wurtzite phase of CdSe (ICSD no. 41825) are shown for comparison in Figure 3c.

PXRD Simulations. The software Powder Cell was used to simulate PXRD patterns (2θ range of 20−75°) by performing a structure factor calculation using lattice parameters, atomic positions, and site

occupancies as input parameters. A space group of 186 (P63mc) was used for the unit cell, and lattice parameters known for bulk wurtzite CdSe (a = 4.29 Å and c = 7.01 Å) were employed. The site occupancies of Cd and Hg ions in the wurtzite lattice were varied to obtain patterns for a range of alloys with Hg fraction, x, ranging from 0 to 0.56, corresponding to the compositions observed in the experimental synthesis. All simulated patterns incorporated Debye–Scherer broadening (fwhm = 2.5° at 2θ = 35°) corresponding to a crystallite size of 3.5 nm. Simulated patterns were then stacked vertically in the order of increasing x in Figure 3d.

Computational Methods. *Parameter and Pseudopotential Usage.* All electronic structure and band structure calculations were performed with plane-wave-basis periodic DFT using the Quantum Espresso[28] software suite. Unless otherwise stated, calculations were performed on bulk wurtzite and zincblende forms of HgSe, CdSe, and $Hg_xCd_{1-x}Se$ alloys using the PBE functional.[66] For all PBE calculations, Norm-conserving Vanderbilt pseudopotentials with spin–orbit coupling, generated using D. R. Hamman's ONCVPSP code,[67,68] were utilized in the final band structure and charge density calculations. The code and input data were both obtained from the publicly available database at quantum-simulation.org. The fully relativistic norm-conserving pseudopotentials used in our final electronic structure calculations were obtained by using the data files that are provided along with the SG15 ONCV potentials as input for the oncvpspr.x code. The input corresponded to the scalar relativistic pseudopotentials Cd_ONCV_PBE-1.0.UPF, Hg_ONCV_PBE-1.0.UPF, and Se_ONCV_PBE-1.1.UPF.

A kinetic energy cutoff of 100 Ry was used along with automatically generated Monkhorst–Pack k-point grids in our calculations. The k-point grid size varied with the size of the crystal basis needed to define each alloy. Alloys with compositions that deviate from 1:1 Hg:Cd ratio require larger numbers of unit cells for structural definition but can be calculated with smaller k-point grids as summarized in Table 2.

Table 2. Summary of Parameters Used for Crystal Basis

system	no. of atoms	no. of unit cells	k-point grid	total energy (eV atom^{-1})
wurtzite CdSe	4	1	6 × 6 × 4	−2243.946348
wurtzite $Hg_{0.25}Cd_{0.75}dSe$	8	2	4 × 4 × 4	−2243.315616
wurtzite $Hg_{0.33}Cd_{0.66}Se$	12	3	3 × 3 × 4	−2243.094773
wurtzite $Hg_{0.5}Cd_{0.5}Se$	4	1	10 × 10 × 10	−2242.694127
wurtzite $Hg_{0.66}Cd_{0.33}Se$	12	3	3 × 3 × 4	−2242.259795
wurtzite $Hg_{0.75}Cd_{0.25}Se$	8	2	4 × 4 × 4	−2242.063034
wurtzite HgSe	4	1	10 × 10 × 10	−2241.442647
zincblende $Hg_{0.25}SCd_{0.75}Se$	8	1	6 × 6 × 6	−2243.320924
zincblende $Hg_{0.375}Cd_{0.625}Se$	16	2	6 × 4 × 6	−2243.007959
zincblende $Hg_{0.5}Cd_{0.5}Se$	8	1	6 × 6 × 6	−2242.695052
zincblende $Hg_{0.625}Cd_{0.375}Se$	16	2	6 × 4 × 6	−2242.383011
zincblende $Hg_{0.75}Cd_{0.25}Se$	8	1	6 × 6 × 6	−2242.071073
zincblende HgSe	2	1	10 × 10 × 10	−2241.448966

The k-point grid dimension is reduced in the direction along which calculation cell is elongated. Convergence tests were performed, as summarized in Table S1 to validate the choice of both the cutoff and grid size parameters. Some of the alloys utilized much larger grids than those needed for convergence simply out of caution at early stages of the study. Marzari-Vanderbilt smearing of 0.0019 Ry, which corresponds to room temperature, was used for the electron occupancies in all the band structure calculations.

Crystal Definition. The unit cell geometry of the wurtzite phase of HgSe was obtained by the relaxation of a starting HgSe unit cell constructed by replacing Cd^{2+} cations in a wurtzite CdSe unit cell[69] with Hg^{2+} cations. This approach was necessitated by the lack of available structural parameters for wurtzite HgSe as this material has not been realized in the bulk. Moreover, our XRD experiments confirm that the lattice parameters of the Hg-containing solids obtained from cation exchange do not differ significantly from those of the initial CdSe template. The relaxation calculations were performed with the scalar relativistic norm-conserving pseudopotentials Hg.pbe-d-hgh.UPF and Se.pbe-hgh.UPF obtained from the Quantum Espresso pseudopotential vault. The zincblende HgSe unit cell geometry was obtained by an initial definition of zincblende HgSe using zincblende CdSe lattice parameters followed by a geometry relaxation performed with the scalar Hg.pbe-d-hgh.UPF and Se.pbe-hgh.UPF pseudopotentials. The resulting zincblende HgSe unit cell showed a lattice constant of 6.26 Å, which matches the experimental known value.[52]

Calculations of the wurtzite CdSe band structure were also performed for comparison. In the relaxed geometry of wurtzite HgSe, Hg^{2+} was replaced with Cd^{2+}, and relaxation was performed using fully relativistic Cd and Se ONCV pseudopotentials. Because no further structural change resulted from this relaxation, the CdSe geometry defined in this manner was employed.

The geometries of the wurtzite $Hg_xCd_{1-x}Se$ alloys were defined using a two-step procedure. First, an initial unit cell geometry of wurtzite $Hg_{0.5}Cd_{0.5}Se$ was defined using the lattice parameters of wurtzite CdSe. This $Hg_{0.5}Cd_{0.5}Se$ unit cell was subject to relaxation. This relaxed unit cell was used to define the geometry for all alloys $Hg_xCd_{1-x}Se$ without any additional relaxation. Cd^{2+} and Hg^{2+} cations were placed in an alternating fashion within the cells to achieve as even a distribution as possible. Zincblende $Hg_xCd_{1-x}Se$ alloys were defined using the relaxed zincblende HgSe unit cell geometry without further relaxation. All relaxations were conducted using the default values in the CELL and IONS namelists of the PWSCF input.

Band Structure and Effective Mass Calculations. Band structures were plotted along L → Γ → K high symmetry lines for the wurtzite structures and along the L → Γ → X high symmetry lines for the zincblende structures. The energy vs k-point plots were obtained by following up the initial PWSCF "scf" calculation with a "bands" calculation specified along the high symmetry lines. The Quantum Espresso post processing code bands.x was then used to print the energy v.s. k-point bands data.

Effective electron and hole masses were calculated for wurtzite structures from band structure plots in Origin Lab software. k-points were first converted into inverse real-space coordinates. A 1000-point B-spline interpolation of the band structure data was performed separately along two different high symmetry lines: −L → Γ → L and −K → Γ → K. The second derivative of the energy with respect to k was then calculated by a finite difference method as

$$E'(k) = \frac{0.5(E(k + \Delta k) - E(k))}{\Delta k} + \frac{0.5(E(k) - E(k - \Delta k))}{\Delta k} \tag{3}$$

$$E''(k) = \frac{0.5(E'(k + \Delta k) - E'(k))}{\Delta k} + \frac{0.5(E'(k) - E'(k - \Delta k))}{\Delta k} \tag{4}$$

where Δk is the k-point spacing. The second derivative at the Γ point was obtained by averaging over a finite range about the Γ point. This range was kept smaller than 10% of the full k-point range. Effective carrier masses used to calculate the size-modified band gaps are averages of the effective masses calculated about Γ along the two high symmetry lines.

Calculation of NC Band Gaps. Values for the NC optical band gap were calculated (eq 2) by accounting for quantum confinement and exciton binding.[70] Bulk high-frequency dielectric constants for CdSe (ε_{CdSe} = 6.32)[71] and HgSe (ε_{HgSe} = 17)[72] were obtained from literature. For the alloys, high-frequency dielectric constants were estimated for different Hg fraction x as

$$\varepsilon_{alloy} = \varepsilon_{HgSe}*(x) + \varepsilon_{CdSe}*(1-x) \tag{6}$$

NC dielectric constants were approximated from the bulk values as in literature.[73]

$$\varepsilon_{NC} = \frac{1 + (\varepsilon_{bulk} - 1)}{[1 + (7.5\text{Å}/D_{NC})^{1.2}]} \tag{7}$$

The bulk band gap of wurtzite CdSe was obtained from a separate hybrid functional PBE0 calculation with a $6 \times 6 \times 6$ Monkhorst−Pack grid and 100 Ry plane-wave basis cutoff. Cd.pbe-d-hgh.UPF and Se.pbe-hgh.UPF pseudopotentials from the Quantum Espresso vault were used. This calculation yielded a band gap of 1.763 eV, in good agreement with the experimental value. A hybrid functional calculation was employed only for CdSe as it has a conventional semiconductor band gap known to be underestimated by the PBE functional.[32] The other $Hg_xCd_{1−x}Se$ alloys are predicted to have inverted band structures with band gaps that originate from crystal splitting, as mentioned in the main text. Thus, hybrid functionals were not needed to ensure the accuracy of the alloy band gaps. It must be noted that the unit cell geometry employed for the PBE0 calculation differed slightly from that of all other cells because it was produced by a separate PBE variable cell relaxation starting from the ideal wurtzite parameters.[69] A 100 Ry cutoff and a $20 \times 20 \times 20$ Monkhorst−Pack k-point grid was used for this relaxation. The Cd.pbe-d-hgh.UPF and Se.pbe-hgh.UPF pseudopentials obtained from the Quantum Espresso vault were employed. The relaxed CdSe cell did not deviate far from the ideal structure and did not differ significantly from the other relaxed wurtzite cells.

The effective hole and electron masses for CdSe and all alloys were obtained from nonhybrid PBE functional band structure calculations.

Band Orbital Character Calculations. Orbital character contributions were obtained by integrating projected density of states (PDOS) data at the Γ point for each alloy species using the trapezoid method. The k-resolved PDOS data itself was obtained with the Quantum Espresso projwfc.x code using an energy grid spacing of 0.001 eV. PDOS data was generated for the s, p, and d atomic states of each individual Cd, Hg, and Se atom in the calculation cell. The PDOS was summed across all atoms of an element to obtain the total s, p, and d atomic state contribution for each element: Cd, Hg, or Se. Final orbital character contributions were obtained by integrating the element-wise PDOS in an energy range corresponding to either the Γ_7 SO band or the hole bands. The integration ranges were obtained by inspecting the base of the DOS peaks, making sure that the range covered the whole peak. The Γ_8 lh and Γ_8 hh bands were not distinguished due to the significant overlap of their DOS peaks, and orbital character contributions are calculated for them jointly and identified as the "holes" bands. The orbital character contribution is the fraction of the total Γ_7 SO band or hole band peak area contributed by s, p, or d atomic states of the three elements.

Charge Density Map Generation. Charge density maps were obtained via postprocessing with the Quantum Espresso pp.x code and subsequently visualized with the XCrySDen visualization program. Isosurface values that allowed for the best visualization of key charge distribution features and orbital character were used to generate maps.

ASSOCIATED CONTENT

Ⓢ Supporting Information

The Supporting Information is available free of charge on the ACS Publications website at DOI: 10.1021/acs.chemmater.7b01674.

> NC size analysis, convergence test results, band structures of all alloys investigated, orbital character plots as a function of x, effect of compositional anisotropy on the band structure, and effect of composition variations on the NC band gap trend (PDF)

AUTHOR INFORMATION

Corresponding Author
*E-mail: jain@illinois.edu.

ORCID Ⓘ
Prashant K. Jain: 0000-0002-7306-3972

Author Contributions
D.D.T. designed simulations, performed simulations and analysis, developed models, and wrote the manuscript. P.B. conducted materials synthesis and characterization, performed analysis, and cowrote the manuscript. S. P. provided computational resources and proofread the manuscript. P.K.J. conceived the project, designed experiments and models, performed supporting simulations, analyzed data, and wrote the manuscript.

Notes
The authors declare no competing financial interest.

REFERENCES

(1) Bernevig, B. A.; Hughes, T. L.; Zhang, S.-C. Quantum Spin Hall Effect and Topological Phase Transition in HgTe Quantum Wells. *Science* **2006**, *314*, 1757−1761.

(2) Zhang, H.; Liu, C.-X.; Qi, X.-L.; Dai, X.; Fang, Z.; Zhang, S.-C. Topological Insulators in Bi2Se3, Bi2Te3 and Sb2Te3 with a Single Dirac Cone on the Surface. *Nat. Phys.* **2009**, *5*, 438−442.

(3) Fu, L.; Kane, C. L. Superconducting Proximity Effect and Majorana Fermions at the Surface of a Topological Insulator. *Phys. Rev. Lett.* **2008**, *100*, 096407.

(4) Akhmerov, A. R.; Nilsson, J.; Beenakker, C. W. J. Electrically Detected Interferometry of Majorana Fermions in a Topological Insulator. *Phys. Rev. Lett.* **2009**, *102*, 216404.

(5) Li, Z.-Z.; Zhang, F.-C.; Wang, Q.-H. Majorana Modes in a Topological Insulator/S-Wave Superconductor Heterostructure. *Sci. Rep.* **2015**, *4*, 6363.

(6) Hesjedal, T.; Chen, Y. Topological Insulators: Engineered Heterostructures. *Nat. Mater.* **2016**, *16*, 3−4.

(7) Hasan, M. Z.; Kane, C. L. Colloquium: Topological Insulators. *Rev. Mod. Phys.* **2010**, *82*, 3045−3067.

(8) Qi, X.-L.; Zhang, S.-C. Topological Insulators and Superconductors. *Rev. Mod. Phys.* **2011**, *83*, 1057−1110.

(9) Park, C.-H.; Yang, L.; Son, Y.-W.; Cohen, M. L.; Louie, S. G. Anisotropic Behaviours of Massless Dirac Fermions in Graphene under Periodic Potentials. *Nat. Phys.* **2008**, *4*, 213−217.

(10) Lin, H.; Wray, L. A.; Xia, Y.; Xu, S.; Jia, S.; Cava, R. J.; Bansil, A.; Hasan, M. Z. Half-Heusler Ternary Compounds as New Multifunctional Experimental Platforms for Topological Quantum Phenomena. *Nat. Mater.* **2010**, *9*, 546−549.

(11) König, M.; Wiedmann, S.; Brüne, C.; Roth, A.; Buhmann, H.; Molenkamp, L. W.; Qi, X.-L.; Zhang, S.-C. Quantum Spin Hall Insulator State in HgTe Quantum Wells. *Science* **2007**, *318*, 766−770.

(12) Fu, L.; Kane, C. L. Topological Insulators with Inversion Symmetry. *Phys. Rev. B: Condens. Matter Mater. Phys.* **2007**, *76*, 045302.

(13) Moore, J. E. The Birth of Topological Insulators. *Nature* **2010**, *464*, 194−198.

(14) Barfuss, A.; Dudy, L.; Scholz, M. R.; Roth, H.; Höpfner, P.; Blumenstein, C.; Landolt, G.; Dil, J. H.; Plumb, N. C.; Radovic, M.; et al. Elemental Topological Insulator with Tunable Fermi Level: Strained α-Sn on InSb(001). *Phys. Rev. Lett.* **2013**, *111*, 157205.

(15) Brüne, C.; Liu, C. X.; Novik, E. G.; Hankiewicz, E. M.; Buhmann, H.; Chen, Y. L.; Qi, X. L.; Shen, Z. X.; Zhang, S. C.; Molenkamp, L. W. Quantum Hall Effect from the Topological Surface States of Strained Bulk HgTe. *Phys. Rev. Lett.* **2011**, *106*, 126803.

(16) Chu, R.-L.; Shan, W.-Y.; Lu, J.; Shen, S.-Q. Surface and Edge States in Topological Semimetals. *Phys. Rev. B: Condens. Matter Mater. Phys.* **2011**, *83*, 075110.

(17) Biering, S.; Schwerdtfeger, P. A comparative density functional study of the low pressure phases of solid ZnX, CdX, and HgX: Trends and relativistic effects. *J. Chem. Phys.* **2012**, *136*, 034504.

(18) Biering, S.; Schwerdtfeger, P. A comparative density functional study of the high-pressure phases of solid ZnX, CdX, and HgX: Trends and relativistic effects. *J. Chem. Phys.* **2012**, *137*, 034705.

(19) White, S. L.; Smith, J. G.; Behl, M.; Jain, P. K. Co-Operativity in a Nanocrystalline Solid-State Transition. *Nat. Commun.* **2013**, *4*, 2933.

(20) Rivest, J. B.; Jain, P. K. Cation Exchange on the Nanoscale: An Emerging Technique for New Material Synthesis, Device Fabrication, and Chemical Sensing. *Chem. Soc. Rev.* **2013**, *42*, 89−96.

(21) Li, H.; Zanella, M.; Genovese, A.; Povia, M.; Falqui, A.; Giannini, C.; Manna, L. Sequential Cation Exchange in Nanocrystals: Preservation of Crystal Phase and Formation of Metastable Phases. *Nano Lett.* **2011**, *11*, 4964−4970.

(22) Robinson, R. D.; Sadtler, B.; Demchenko, D. O.; Erdonmez, C. K.; Wang, L.-W.; Alivisatos, A. P. Spontaneous Superlattice Formation in Nanorods through Partial Cation Exchange. *Science* **2007**, *317*, 355−358.

(23) Harman, T. C.; Strauss, A. J. Band Structure of HgSe and HgSe−HgTe Alloys. *J. Appl. Phys.* **1961**, *32*, 2265−2270.

(24) Xu, L.; Chen, K.; Zhu, J.; Chen, H.; Huang, H.; Xu, J.; Huang, X. Core-Shell Structure and Quantum Effect of CdSe/HgSe/CdSe Quantum Dot Quantum Well. *Superlattices Microstruct.* **2001**, *29*, 67−72.

(25) Svane, A.; Christensen, N. E.; Cardona, M.; Chantis, A. N.; van Schilfgaarde, M.; Kotani, T. Quasiparticle Band Structures of β-HgS, HgSe, and HgTe. *Phys. Rev. B: Condens. Matter Mater. Phys.* **2011**, *84*, 205205.

(26) Sakuma, R.; Friedrich, C.; Miyake, T.; Blügel, S.; Aryasetiawan, F. GW Calculations Including Spin-Orbit Coupling: Application to Hg Chalcogenides. *Phys. Rev. B: Condens. Matter Mater. Phys.* **2011**, *84*, 085144.

(27) Efros, A. L.; Rosen, M. The Electronic Structure of Semiconductor Nanocrystals. *Annu. Rev. Mater. Sci.* **2000**, *30*, 475−521.

(28) Giannozzi, P.; Baroni, S.; Bonini, N.; Calandra, M.; Car, R.; Cavazzoni, C.; Ceresoli, D.; Chiarotti, G. L.; Cococcioni, M.; Dabo, I.; et al. QUANTUM ESPRESSO: A Modular and Open-Source Software Project for Quantum Simulations of Materials. *J. Phys.: Condens. Matter* **2009**, *21*, 395502.

(29) Li, J.; Wang. Electronic Structure of InP Quantum Rods: Differences between Wurtzite, Zinc Blende, and Different Orientations. *Nano Lett.* **2004**, *4*, 29−33.

(30) Hopfield, J. J. Fine Structure in the Optical Absorption Edge of Anisotropic Crystals. *J. Phys. Chem. Solids* **1960**, *15*, 97−107.

(31) Chen, Y. L.; Analytis, J. G.; Chu, J.-H.; Liu, Z. K.; Mo, S.-K.; Qi, X. L.; Zhang, H. J.; Lu, D. H.; Dai, X.; Fang, Z.; et al. Experimental Realization of a Three-Dimensional Topological Insulator, Bi2Te3. *Science* **2009**, *325*, 178−181.

(32) Szemjonov, A.; Pauporté, T.; Ciofini, I.; Labat, F. Investigation of the Bulk and Surface Properties of CdSe: Insights from Theory. *Phys. Chem. Chem. Phys.* **2014**, *16*, 23251−23259.

(33) Ninomiya, S.; Adachi, S. Optical Properties of Cubic and Hexagonal CdSe. *J. Appl. Phys.* **1995**, *78*, 4681−4689.

(34) Mocatta, D.; Cohen, G.; Schattner, J.; Millo, O.; Rabani, E.; Banin, U. Heavily Doped Semiconductor Nanocrystal Quantum Dots. *Science* **2011**, *332*, 77−81.

(35) Mu, L.; Wang, F.; Sadtler, B.; Loomis, R. A.; Buhro, W. E. Influence of the Nanoscale Kirkendall Effect on the Morphology of Copper Indium Disulfide Nanoplatelets Synthesized by Ion Exchange. *ACS Nano* **2015**, *9*, 7419−7428.

(36) Jain, P. K.; Amirav, L.; Aloni, S.; Alivisatos, A. P. Nanoheterostructure Cation Exchange: Anionic Framework Conservation. *J. Am. Chem. Soc.* **2010**, *132*, 9997−9999.

(37) Jain, P. K.; Beberwyck, B. J.; Fong, L.-K.; Polking, M. J.; Alivisatos, A. P. Highly Luminescent Nanocrystals From Removal of Impurity Atoms Residual From Ion-Exchange Synthesis. *Angew. Chem., Int. Ed.* **2012**, *51*, 2387−2390.

(38) Routzahn, A. L.; Jain, P. K. Single-Nanocrystal Reaction Trajectories Reveal Sharp Cooperative Transitions. *Nano Lett.* **2014**, *14*, 987−992.

(39) Routzahn, A. L.; Jain, P. K. Luminescence Blinking of a Reacting Quantum Dot. *Nano Lett.* **2015**, *15*, 2504−2509.

(40) White, S. L.; Banerjee, P.; Chakraborty, I.; Jain, P. K. Ion Exchange Transformation of Magic-Sized Clusters. *Chem. Mater.* **2016**, *28*, 8391−8398.

(41) White, S. L.; Banerjee, P.; Jain, P. K. Liquid-like Cationic Sub-Lattice in Copper Selenide Clusters. *Nat. Commun.* **2017**, *8*, 14514.

(42) Wark, S. E.; Hsia, C.-H.; Son, D. H. Effects of Ion Solvation and Volume Change of Reaction on the Equilibrium and Morphology in Cation-Exchange Reaction of Nanocrystals. *J. Am. Chem. Soc.* **2008**, *130*, 9550−9555.

(43) Luther, J. M.; Zheng, H.; Sadtler, B.; Alivisatos, A. P. Synthesis of PbS Nanorods and Other Ionic Nanocrystals of Complex Morphology by Sequential Cation Exchange Reactions. *J. Am. Chem. Soc.* **2009**, *131*, 16851−16857.

(44) Ott, F. D.; Spiegel, L. L.; Norris, D. J.; Erwin, S. C. Microscopic Theory of Cation Exchange in CdSe Nanocrystals. *Phys. Rev. Lett.* **2014**, *113*, 156803.

(45) Son, D. H.; Hughes, S. M.; Yin, Y.; Alivisatos, A. P. Cation Exchange Reactions in Ionic Nanocrystals. *Science* **2005**, *36*, 1009−1012.

(46) Routzahn, A. L.; White, S. L.; Fong, L.-K.; Jain, P. K. Plasmonics with Doped Quantum Dots. *Isr. J. Chem.* **2012**, *52*, 983−991.

(47) Tolbert, S. H.; Alivisatos, A. P. Size Dependence of a First Order Solid-Solid Phase Transition: The Wurtzite to Rock Salt Transformation in CdSe Nanocrystals. *Science* **1994**, *265*, 373−376.

(48) Carbone, L.; Nobile, C.; De Giorgi, M.; Sala, F. D.; Morello, G.; Pompa, P.; Hytch, M.; Snoeck, E.; Fiore, A.; Franchini, I. R.; et al. Synthesis and Micrometer-Scale Assembly of Colloidal CdSe/CdS Nanorods Prepared by a Seeded Growth Approach. *Nano Lett.* **2007**, *7*, 2942−2950.

(49) Smith, A. M.; Nie, S. Bright and Compact Alloyed Quantum Dots with Broadly Tunable Near-Infrared Absorption and Fluorescence Spectra through Mercury Cation Exchange. *J. Am. Chem. Soc.* **2011**, *133*, 24−26.

(50) Smith, A. M.; Lane, L. A.; Nie, S. Mapping the Spatial Distribution of Charge Carriers in Quantum-Confined Heterostructures. *Nat. Commun.* **2014**, *5*, 4506.

(51) Gupta, S.; Kershaw, S. V.; Susha, A. S.; Wong, T. L.; Higashimine, K.; Maenosono, S.; Rogach, A. L. Near-Infrared-Emitting $Cd_XHg_{1−X}$ Se Nanorods Fabricated by Ion Exchange in an Aqueous Medium. *ChemPhysChem* **2013**, *14*, 2853−2858.

(52) Wyckoff, R. W. G. *Crystal Structures*; R.E. Krieger Pub. Co.: Malabar, Florida, 1982.

(53) Milliron, D. J.; Hughes, S. M.; Cui, Y.; Manna, L.; Li, J.; Wang, L.-W.; Paul Alivisatos, A. Colloidal Nanocrystal Heterostructures with Linear and Branched Topology. *Nature* **2004**, *430*, 190−195.

(54) Stein, T.; Kronik, L.; Baer, R. Reliable Prediction of Charge Transfer Excitations in Molecular Complexes Using Time-Dependent Density Functional Theory. *J. Am. Chem. Soc.* **2009**, *131*, 2818−2820.

(55) Pietryga, J. M.; Werder, D. J.; Williams, D. J.; Casson, J. L.; Schaller, R. D.; Klimov, V. I.; Hollingsworth, J. A. Utilizing the Lability

of Lead Selenide to Produce Heterostructured Nanocrystals with Bright, Stable Infrared Emission. *J. Am. Chem. Soc.* **2008**, *130*, 4879−4885.

(56) De Trizio, L.; Manna, L. Forging Colloidal Nanostructures via Cation Exchange Reactions. *Chem. Rev.* **2016**, *116*, 10852−10887.

(57) Alivisatos, A. P. Semiconductor Clusters, Nanocrystals, and Quantum Dots. *Science* **1996**, *271*, 933−937.

(58) Luttinger, J. M.; Kohn, W. Motion of Electrons and Holes in Perturbed Periodic Fields. *Phys. Rev.* **1955**, *97*, 869−883.

(59) Koole, R.; Groeneveld, E.; Vanmaekelbergh, D.; Meijerink, A.; Donegá, C. de M. Size Effects on Semiconductor Nanoparticles. In *Nanoparticles*; Donegá, C. de M., Ed.; Springer: Berlin, Heidelberg, 2014; pp 13−51.

(60) Yu, P.; Cardona, M. *Fundamentals of Semiconductors: Physics and Materials Properties*; Springer Science & Business Media: New York, 2005.

(61) Alivisatos, A. P. Perspectives on the Physical Chemistry of Semiconductor Nanocrystals. *J. Phys. Chem.* **1996**, *100*, 13226−13239.

(62) Sessi, P.; Di Sante, D.; Szczerbakow, A.; Glott, F.; Wilfert, S.; Schmidt, H.; Bathon, T.; Dziawa, P.; Greiter, M.; Neupert, T.; et al. Robust Spin-Polarized Midgap States at Step Edges of Topological Crystalline Insulators. *Science* **2016**, *354*, 1269−1273.

(63) Siroki, G.; Lee, D. K. K.; Haynes, P. D.; Giannini, V. Single-Electron Induced Surface Plasmons on a Topological Nanoparticle. *Nat. Commun.* **2016**, *7*, 12375.

(64) Yoshimura, Y.; Kobayashi, K.; Ohtsuki, T.; Imura, K.-I. Engineering Dirac Electrons Emergent on the Surface of a Topological Insulator. *Sci. Technol. Adv. Mater.* **2015**, *16*, 014403.

(65) Allan, G.; Delerue, C. Tight-Binding Calculations of the Optical Properties of HgTe Nanocrystals. *Phys. Rev. B: Condens. Matter Mater. Phys.* **2012**, *86*, 165437.

(66) Perdew, J. P.; Burke, K.; Ernzerhof, M. Generalized Gradient Approximation Made Simple. *Phys. Rev. Lett.* **1996**, *77*, 3865−3868.

(67) Hamann, D. R. Optimized Norm-Conserving Vanderbilt Pseudopotentials. *Phys. Rev. B: Condens. Matter Mater. Phys.* **2013**, *88*, 085117.

(68) Schlipf, M.; Gygi, F. Optimization Algorithm for the Generation of ONCV Pseudopotentials. *Comput. Phys. Commun.* **2015**, *196*, 36−44.

(69) Zakharov, O.; Rubio, A.; Cohen, M. L. Calculated Structural and Electronic Properties of CdSe under Pressure. *Phys. Rev. B: Condens. Matter Mater. Phys.* **1995**, *51*, 4926−4930.

(70) Jasieniak, J.; Califano, M.; Watkins, S. E. Size-Dependent Valence and Conduction Band-Edge Energies of Semiconductor Nanocrystals. *ACS Nano* **2011**, *5*, 5888−5902.

(71) Pellegrini, G.; Mattei, G.; Mazzoldi, P. Finite depth square well model: Applicability and limitations. *J. Appl. Phys.* **2005**, *97*, 073706.

(72) Manabe, A.; Mitsuishi, A. Far-Infrared Reflection Spectra of HgSe. *Solid State Commun.* **1975**, *16*, 743−745.

(73) Wang, L.; Zunger, A. Pseudpotential calculations of nanoscale CdSe quantum dots. *Phys. Rev. B: Condens. Matter Mater. Phys.* **1996**, *53*, 9579−9582.